THE JOURNAL OF BIOLOGICAL CHEMISTRY VOL. 286, NO. 4, pp. 3079–3093, January 28, 2011
Printed in the U.S.A.

Ectopic Mineralization in the Middle Ear and Chronic Otitis Media with Effusion Caused by *RPL38* Deficiency in the Tail-short (*Ts*) Mouse*[S]

Received for publication, September 13, 2010, and in revised form, November 5, 2010 Published, JBC Papers in Press, November 9, 2010, DOI 10.1074/jbc.M110.184598

Konrad Noben-Trauth[1] **and Joseph R. Latoche**

From the Section on Neurogenetics, Laboratory of Molecular Biology, NIDCD, National Institutes of Health, Rockville, Maryland 20850

Inflammation of the middle ear cavity (otitis media) and the abnormal deposition of bone at the otic capsule are common causes of conductive hearing impairment in children and adults. Although a host of environmental factors can contribute to these conditions, a genetic predisposition has an important role as well. Here, we analyze the Tail-short (*Ts*) mouse, which harbors a spontaneous semi-dominant mutation that causes skeletal defects and hearing loss. By genetic means, we show that the *Ts* phenotypes arise from an 18-kb deletion/insertion of the *Rpl38* gene, encoding a ribosomal protein of the large subunit. We show that *Ts* mutants exhibit significantly elevated auditory-brain stem response thresholds and reduced distortion-product otoacoustic emissions, in the presence of normal endocochlear potentials and typical inner ear histology suggestive of a conductive hearing impairment. We locate the cause of the hearing impairment to the middle ear, demonstrating over-ossification at the round window ridge, ectopic deposition of cholesterol crystals in the middle ear cavity, enlarged Eustachian tube, and chronic otitis media with effusion all beginning at around 3 weeks after birth. Using specific antisera, we demonstrate that Rpl38 is an ~8-kDa protein that is predominantly expressed in mature erythrocytes. Finally, using an *Rpl38* cDNA transgene, we rescue the *Ts* phenotypes. Together, these data present a previously uncharacterized combination of interrelated middle ear pathologies and suggest *Rpl38* deficiency as a model to dissect the causative relationships between neo-ossification, cholesterol crystal deposition, and Eustachian tubes in the etiology of otitis media.

The otic capsule, also called the cochlear capsule or bony labyrinth, encloses the membranous inner ear. It develops through condensation of mesenchymal cells surrounding the otic vesicle, which form a chondrified capsule that ossifies during the late embryonic and early postnatal period (1). The bone of the mature otic capsule, which constitutes the petrous part of the temporal bone, consists of the inner endosteal, the middle endochondral, and the outer (facing the middle ear cavity) periosteal layer (2). Metabolically, this bone is largely inert with an unusually low remodeling rate of <2% per year (3). Pathological formation of new bone is the hallmark of both otosclerosis and labyrinthitis ossificans. In otosclerosis, abnormal deposition of bone occurs most often outside of the otic capsule at the base and near the oval and round windows (4). In contrast, neo-ossification in labyrinthitis ossificans manifests within the otic capsule and in the membranous labyrinth (5). Although the causes of otosclerosis include environmental and genetic factors (6, 7), labyrinthitis ossificans typically results from an infection or chronic inflammation (5, 8).

Connected to the otic capsule is the middle ear, whose skeletal components are derived from the neural crest that gave rise to the pharyngeal arches and pouches (9). The endodermal lining of the first pharyngeal pouch develops into the tubotympanic recess that further differentiates into the Eustachian tube and middle ear cavity (10).

Otitis media (OM)[2] refers to the inflammation of the middle ear cavity. It is classified based upon its clinical severity and is the most common childhood disease. More than 83% of children have experienced at least one episode of OM, although 46% of children have had more than three incidents by the age of 3 (11). Various stages of OM can be diagnosed and include acute otitis media, otitis media with effusion (OME), and chronic suppurative otitis media (CSOM). Children with recurrent episodes of acute otitis media and those developing CSOM or OME have higher risks of developing conductive and sensorineural hearing loss (12–14). There are multiple causes and risk factors associated with OM, which can include bacterial and viral infections, craniofacial dysmorphologies, and dysregulated immune responses (15). There is also considerable evidence for a genetic predisposition. For example, a heritability study found strong genetic contributions for the duration and number of episodes of OM in monozygotic twins and triplets (16). In addition, genome-wide linkage scans produced evidence for susceptibility loci on chromosomes 17q12, 10q22.3, and 19q13 associated with chronic and recurrent OM (17, 18). Furthermore, targeted and induced mutagenesis identified mouse lines that model the pathology of OME (*Eya4*^{tm1Jse}) and CSOM (*Fbxo11*^{A2288T} and *Evi1*^{A1427T}) (19–21). In these models, mutations in the

* This work was supported, in whole or in part, by National Institutes of Health Division of Intramural Research.

[S] The on-line version of this article (available at http://www.jbc.org) contains supplemental Table S1 and Figs. S1–S3.

[1] To whom correspondence should be addressed: 5 Research Ct., Rockville, MD 20850. Fax: 301-435-4040; E-mail: nobentk@nidcd.nih.gov.

[2] The abbreviations used are: OM, otitis media; ABR, auditory-brain stem response; DPOAE, distortion-product otoacoustic emission; EP, endocochlear potential; OME, otitis media with effusion; CSOM, chronic suppurative otitis media; ET, Eustachian tube; SPL, sound pressure level.

transcription factor Eya4 and ubiquitination factor Fxbo11 cause dysmorphologies of the Eustachian tube (ET), suggesting that impaired aeration of the middle ear cavity and clearance of the middle ear secretions is the underlying cause of the OM. Inflammation of the middle ear was also observed in the *N*-ethyl-*N*-nitrosourea induced Hush Puppy mutant, in plasminogen-deficient mice (Plg^{tm1Dco}), and mice of the LP/J inbred strain further underscoring the diverse and complex etiology of otitis media (22–25).

The Tail-short (*Ts*) mutation, first described by Morgan (26), is characterized by a shortened, kinked tail and reduced body weight. *Ts* homozygotes are embryonic lethal and die between gestation day E3.5 and E5.5 (27). *Ts* heterozygotes undergo a transient embryonic anemia, which is accompanied by a protracted growth and the formation of skeletal abnormalities (28, 29). The mutation arose originally on the BALB/c background and has been crossed onto C57BL/6, C56BR/a, and BALB/cSn before it was made inbred to give rise to the TSJ/LeJ-*Ts* strain. The severity of the *Ts* allele varies on different genetic backgrounds, but even on the most permissive strains 30% of the *Ts* heterozygotes are perinatal lethal (26, 30). Skeletal deformities are known to be accompanied by defects in the inner ear in the mouse (31, 32). To determine the effect of *Ts* on the perception and propagation of sound, we set out to clone the *Ts* locus and study the ear phenotype.

MATERIALS AND METHODS

Animals and Crosses—The TSJ/Le and C3HeB/FeJ strains were obtained from The Jackson Laboratory (Bar Harbor, ME) and Black Swiss mice were purchased from Taconic. For audiology, histology, and immunochemistry, TSJ/LeJ-*Ts/+* (*Ts/+* or *Ts*) and TSJ/LeJ-+/+ (+/+) mice were used. For the F2 linkage, cross-reciprocal matings between TSJ/Le-*Ts/+* and Black Swiss mice were used to generate *Ts/+* F1 heterozygotes (TsJ/LeJ.BlackSwiss-*Ts/+*), which were intercrossed to produce 1684 F2 progeny. For the rescue, transgenic founders on the FVB/N background were serially backcrossed to TSJ/Le-*Ts/+*. Animal studies were conducted according to guidelines of the National Institutes of Health (ASP 1222).

Molecular Genetics Techniques—For genotyping of fluorescence-labeled markers, 20–50 ng of genomic DNA was amplified in a 10-μl reaction containing 0.1 μM each primer, 200 μM dNTP, 10 mM Tris-HCl, pH 8.3, 50 mM KCl, 1.5 mM $MgCl_2$, and 0.25 units of AmpliTaq™ DNA polymerase (Applied Biosystems). Reaction was incubated at 95 °C for 1 min and then cycled 50 times through 95 °C for 45 s, 55 °C for 1 min, and 72 °C for 1 min, followed by a final extension at 72 °C for 10 min. For electrophoresis, 1 μl of amplified product was diluted 1:10 in formamide containing 0.1 μl of GenScan™ 500 ROX™ size standard, separated on a 3730 DNA Analyzer (Applied Biosystems), and analyzed using GenMapper software version 3.1 (Applied Biosystems). Primer sequences are available upon requests.

To screen the *Ts* interval for large scale insertions/deletions, forward and reverse primers spanning the region at 1-kb intervals were synthesized, and all combinations were used in a 10-μl reaction containing 50–100 ng +/+ or *Ts*/+ genomic DNA, using the Takara Bio LA TaqDNA polymerase kit (Takara, Madison, WI). Amplification was carried out at 94 °C for 1 min and then cycled 30 times through 94 °C for 30 s, 60 °C for 30 s, and 72 °C for 3 min, followed by a final extension at 72 °C for 7 min. The *Ts* deletion was detected using forward primer TsJ-27F (CAAGACACATCTGGAGTCACAGGG) and reverse primers that included chr11-C31-r (CCTGGAACTCATTATGTAGAGCAGC), chr11-C32-r (ATGGTGCGTGCCTTAGGATGG), chr11-C34-r (AAGAGAGAAAGGAGTGGGACCTGGG), chr11-C36-r (GCAGCCTTTGTGAAGAAGCC), and chr11-C38-r (GCCCCACTATGGAGATTAGGAC). *Ts* mice were genotyped by PCR on genomic DNA using primer del-a-f (GCTTTTGGAAACTCGGTCAC) and del-b-r (CCAGTTTCCTGTCTTTCCACG) flanking the deletion site in a 10-μl reaction using the Clontech cDNA PCR polymerase mix.

For DNA sequencing, PCR was performed in a 15-μl reaction containing 50–100 ng of genomic DNA, 200 μM dNTP, 2 μM each forward and reverse primers, and 1× Advantage cDNA polymerase mix (Clontech). Amplification was carried out following the manufacturer's instructions. Reactions were treated with 1 unit of shrimp alkaline phosphatase (Roche Applied Science) and 1 unit of exonuclease (New England Biolabs) at 37 °C for 60 min and inactivated at 80 °C for 10 min. Sequencing of PCR products was performed using BigDye® Terminator version 3.1 and electrophoresed on a 3730xl capillary sequencer (Applied Biosystems). Sequence chromatograms were analyzed using Sequencher version 4.1. Primer sequences are available upon request.

Hearing Tests—Hearing tests were performed on mice anesthetized through intraperitoneal application of tribromoethanol (5.3 mg/10 g of body weight). Auditory-evoked brain stem response (ABR) measurements were carried out using the computer-aided evoked potential system from Intelligent Hearing System (Miami, Florida). The Smart-EP version 10, modified for high frequency capability and coupled to high frequency transducers, generated specific acoustic stimuli and to amplify, measure, and display the evoked brainstem responses of anesthetized mice. Subdermal needle electrodes were inserted at the vertex (active), ventrolaterally to the right ear (reference) and the left ear (ground). Specific acoustic stimuli were delivered to the outer ear canal through a plastic tube channeled from the high frequency transducers. Mice were presented with click stimuli and with 8-, 16-, and 32-kHz tone pips at varying intensity, from high to low (100–10 db SPL) at a rate of 19.1 times/s for a total of 350 sweeps. Sound pressure level thresholds were determined for each stimulus frequency by identifying the lowest intensity producing a recognizable ABR pattern of the computer screen (at least two consistent characteristic wave forms).

Distortion-product otoacoustic emissions (DPOAEs) were measured using LabView 8.6 software (National Instruments), operating an PCI-4461 dynamic signal analyzer sound card (National Instruments) to generate two pure tones, f1 and f2, at the fixed f2/f1 ratio of 1.25, which were emitted separately by two Clarion SRU310H high frequency dome tweeters placed in the outer ear canal at the presentation level of f2 =

f1 (sound pressure level). The f2 component was swept in 1-kHz steps starting from f2 = 5 to 55 kHz. Intensity levels sweeps ranged from 15 db SPL up to 75 db SPL, in 10 db increments. Sound pressure levels were measured using an Etymõtic-ER-10B+ microphone. The amplitude of the 2f1-f2 distortion product was plotted in decibel of SPL against the f2 frequency where the distortion product is generated. Clarion speakers and Etymõtic ER-10B+ microphone were calibrated using a ¼-inch microphone 7016 (¼-inch pre-amp 4016 and microphone power supply PS9200, AcoPacific). The AcoPacific ¼-inch microphone 7016 was calibrated using a QC-10 sound calibrator (Quest Technologies).

The EP was measured via the round window. Briefly, the tip of a small glass pipette containing a silver/chloride electrode bathed in 0.1 M KCl was inserted through the round window into the endolymph using a remote-controlled motorized micromanipulator (PPM5000, Piezo World Precision Instrument). The electrode was connected to a Warner dual channel differential electrometer (HiZ-223), which amplified and routed the voltage difference (subdermal 1 M KCl reference electrode) to a PC-controlled data acquisition system (Digidata 1440A, Axon Instruments) using AxoScope software, which displayed the measured output. Data were sampled at a rate of 10 kHz for 60 s. The glass electrode was prepared using a Sutter Instrument (P-97 Flaming/Brown micropipette puller), and measurements were performed in a bench top Faraday cage (Technical Manufacturing Corp.).

Antibodies—Polyclonal rabbit Rpl38-specific antisera were generated against synthetic peptides (Pb863, TARRKDAKSVKIKKNKDNV amino acids 14–32; Pb865, LVITDKEKAEKLKQS amino acids 45–59) and affinity-purified. Anti-Myc antibody was obtained from OriGene.

Histology and Immunohistochemistry—For gross morphology on plastic sections, the ear was removed from the temporal bone and dissected in PBS, perfused with 4% paraformaldehyde and kept in the same fixative at room temperature for at least 12 h. Specimens were washed twice in PBS and decalcified in 0.1 M EDTA, pH 7.0, in PBS for 3 weeks. The ears were then dehydrated with a graded series of ethanol, infiltrated with JB-4 monomer (Polysciences, Inc.), and embedded for mid-modiolar and sagittal sections. Serial sections were cut at 4 μm thickness using a tungsten carbide disposable blade on a RM2265 microtome (Leica) and mounted on Superfrost Plus microscope slides. Sections were stained with 0.1% toluidine blue O, destained in 100% EtOH, cleared in xylene, mounted in Permount (Fisher), imaged on a DM5000B microscope (Leica), and photographed with a DFC500 digital camera (Leica). Image levels were adjusted with Adobe Photoshop software. BioVis3D software was used for three-dimensional reconstruction of serial sections.

For immunostaining of organ of Corti whole mounts, cochlear ducts were dissected in Leibovitz medium (Invitrogen) and fixed in 4% paraformaldehyde (Electron Microscopy Sciences) in PBS for 2 h at room temperature. The tectorial membrane was removed, and the tissue was permeabilized in 0.5% Triton X-100 for 30 min at room temperature. It was then washed three times in PBS for 10 min each and stored in blocking solution (5% goat serum, 2% BSA in PBS) at 4 °C overnight. Samples were washed three times and incubated with affinity-purified Pb863 or Pb865 antibodies (1:1000 in blocking solution) for 2 h at room temperature, washed in PBS, and incubated with secondary anti-rabbit IgG antibody (1:1000; Alexa Fluor® 594 donkey; Invitrogen) for 1 h at room temperature. For visualizing the stereociliary bundle, specimens were dissected as described above and stained with rhodamine phalloidin (Invitrogen) diluted 1:100 in PBS for 30 min at room temperature. After washing in PBS, the organ of Corti was removed from the modiolus, mounted in ProLong® Gold antifade reagent with DAPI (Invitrogen), and imaged using a Zeiss LSM confocal microscope.

To generate cryosections of mouse cochlea, ears were fixed as described above. Specimens were washed twice in PBS and equilibrated in a graded series of 5, 10, 15, and 20% sucrose in PBS, then transferred to a 2:1 mixture of 20% sucrose in PBS/OCT medium (Saukra, Torrance, CA), frozen over dry ice and ethanol, then sectioned at 12 μm on a Leica cryostat (CM 3050S), and stored at −80 °C. For immunostaining, cryosections were brought to room temperature in a humidified chamber, then re-fixed in 4% paraformaldehyde in PBS for 15 min, permeabilized in 0.5% Triton X-100 in PBS for 30 min, and stained as described above.

For immunostaining on whole blood, freshly drawn intracardial blood was dispensed into EDTA-K2-coated tubes (Terumo) and rotated for 30 min at room temperature. 50 μl of blood was fixed at 1:2 dilution in 4% paraformaldehyde (Electron Microscopy Sciences), incubated for 10 min at room temperature, and spread onto Superfrost®/Plus microscope slides (Fisher). Slides were air-dried and stored at 4 °C until use. Cells were post-fixed in 4% paraformaldehyde for 10 min at room temperature, washed in PBS, permeabilized in 0.5% Triton X-100 for 30 min, blocked in 5% goat serum, 2% BSA in PBS for 30 min, incubated with either Pb863 (1:200) or Pb865 (1:200) diluted in blocking solution for 60 min, washed and stained with secondary anti-rabbit IgG (1:1000; Alexa Fluor® 594 donkey; Invitrogen) for 60 min, then washed in PBS and mounted in ProLong® Gold antifade reagent (Invitrogen), and imaged on a Zeiss LSM 710 confocal microscope.

Western Blots—Freshly drawn intracardial blood was dispensed into EDTA-K2-coated tubes (Terumo) and rotated for 30 min at room temperature. Cells were diluted 1:15 in Hanks' balanced salt solution, pelleted for 5 min at 3523 relative centrifugal force at 4 °C, washed twice in Hanks' balanced salt solution, resuspended in 200 μl of Hanks' balanced salt solution and frozen in −20 °C until use. Cochleae were dissected in PBS and stored at −20 °C until use.

For Western blot analyses, frozen tissue was lysed in RIPA buffer (50 mM Tris-HCl, pH 7.5, 150 mM NaCl, 1% Triton X-100, 0.5% deoxycholate, 0.1% SDS, 1 mM phenylmethanesulfonyl fluoride (PMSF)) in the presence of Complete protease inhibitor mixture tablets (½-tablet/5 ml of buffer) (Complete, Roche Applied Science) using a motorized homogenizer. Proteins were solubilized for 2 h on ice followed by centrifugation at 4 °C at 20,000 relative centrifugal force for 30 min. Supernatant was collected and stored in aliquots at −20 °C until use. Protein concentrations were deter-

mined using Bradford assay reagents (Bio-Rad). Frozen solubilized protein extracts were thawed on ice, diluted in Laemmli buffer (30 mM Tris-HCl, pH 6.8, 1% SDS, 12.5% glycerol, 0.01% bromphenol blue, 2.5% (v/v) β-mercaptoethanol), and denatured at 70 °C for 10 min. Proteins were separated in 18% NuPAGE™ acrylamide Tris-glycine gels (Invitrogen) at 150 V for 90 min and then transferred onto PVDF membranes in 25 mM Tris, 192 mM glycine, 20% (v/v) methanol using an electrophoretic transfer cell (100 V, 60 min). Rpl38 was detected with Pb863 and Pb865 antibody (1:200 dilution) and alkaline phosphatase-conjugated goat anti-rabbit IgG (1:10,000; Bio-Rad) using chemiluminescence (Bio-Rad). Protein lysates of HEK293T cells transfected with and without Myc-tagged human Rpl38 (NP_001030335) were obtained from OriGene. For the peptide blocking, equal volumes of 10 mg/ml peptide and 1.3 mg/ml Pb865 antibody were mixed and incubated at room temperature for 1 h. For Western blot hybridization and immunohistochemistry staining, antibody/peptide aggregates were diluted 1:200 in blocking solution.

Transgenic Rescue—Poly(A)$^+$ mRNA was extracted from wild type and *Ts*/+ P14 whole cochlea as described and was reverse-transcribed using the SuperScript® II RT system (Clontech). Full-length *RpL38* cDNA was amplified using the forward primer RpL38-mRNA-F4-EcoRI (ATGCGAATTCAGCTCTGTTCTTGAAAAAGACT) and the reverse primer RpL38-mRNA-R2-HindIII (ATGCAAGCTTGTTTTTAATAGTCACACGCAGAGGGC), digested with EcoRI and HindIII, and cloned into pGEM-4Z (construct named pRpL38.1). Coding cDNA was amplified from pRpL38.1 using the forward primer RpL38-pBroad_F1 (ATGCGAATTCGTCGCCATGCCTCGGAAAATTG) and the reverse primer RpL38-pBroad_r1 (GCATGAATTCTCATTTCAGATCCTTCACTGC) (each with engineered EcoRI restriction site) and cloned into pBroad3-MCS (InvivoGen) under the control of the constitutively active mouse ROSA26 promoter (construct named pRpL38.4). The mROSA-RpL38-poly(A) transgene was excised from pRpL38.4 using PacI, purified, and microinjected into FVB/N male pronuclei by the NEI Transgenic Core Facility, National Institutes of Health. Transgenic animals were genotyped by PCR using primers mROSA-Rpl38-F1 (AAGAAGAGGCTGTGCTTTGGG) and Rpl38polyA-R1 (CACAGACAAGGAAAAGGCAGAG) using FailSafe™ PCR system buffer G following manufacturer's instructions (Epicenter Biotechnologies).

Statistical Analyses—Unless otherwise indicated, groups of data were compared using one-way analysis of variance followed by Bonferroni post tests to correct for multiple testing. GraphPad Prism 4.0b software was used to perform the statistics and to plot the data.

RESULTS

Ts Is an Rpl38 Deletion Mutation—Previous linkage analysis placed *Ts* to position 73.5 centimorgans on distal chromosome 11 (33, 34). To further refine this interval, we established an F2 linkage intercross between the parental TSJ/LeJ-*Ts*/+ and Black Swiss strains and produced 3368 meioses. The F2 progeny were classified as either tail-short or normal-tailed based on their tail morphology and genotyped at SSLP markers *D11Mit168*, *D11Mit128*, *D11Mit257*, and *D11Mit203*. This identified 88 recombination events and placed *Ts* between *D11Mit128* and *D11Mit257*. Twenty seven recombinants within this interval were further genotyped using additional single nucleotide polymorphism markers, which ultimately refined the *Ts* locus to a 0.2-centimorgan interval between *D11Ntra3* and *D11Ntra5* (supplemental Fig. S1). This region contains 89,543 bp and is bounded by the MMU11 nucleotides 114,506,775 and 114,596,318 (UCSC Genome Browser on Mouse, July, 2007) (Fig. 1*A*). All known and predicted exons of the three genes within this interval (*RpL38*, *Ttyh2*, and *Dnaic2*) were sequenced, but no polymorphisms were detected between the wild type and *Ts* allele. To test for a large scale insertion and/or deletion mutation, we employed a long range PCR scheme, which revealed the absence of ~18 kb of genomic DNA on the *Ts* chromosome (Fig. 1*B*). DNA sequence analysis of PCR fragments, which were amplified exclusively from the *Ts* chromosome, demonstrated that 18,189 bp containing the entire riboprotein gene *RpL38* had been deleted. Furthermore, the endogenous sequence was replaced with a 657-bp insertion showing high sequence identity to the *gag/pro-pol-dUTPase* genes of the endogenous retrovirus MuERV-L (Fig. 1*C*) (35). PCR analysis of genomic DNA obtained from nine TSJ/Le-+/+ and 13 TSJ/Le-*Ts*/+ mice (including genomic TSJ/Le DNA from The Jackson Laboratory) as well as a number of common inbred strains confirmed that the insertion/deletion mutation is unique to the *Ts* chromosome (Fig. 1*D*).

Elevated ABR Thresholds and Reduced DPOAEs in Ts—To determine the auditory characteristics of *Ts* mice, we measured the neural activity of the cochlear nerve (determining thresholds of ABR), ascertained the functioning of sensory outer hair cells (measuring DPOAEs), and tested the performance of the stria vascularis (measuring the EP).

By employing a series of acoustic stimuli covering a frequency band of six octaves (1–32 kHz), we found a significant increase in ABR thresholds in *Ts* mice. At 4 weeks of age, thresholds at the click and 8 kHz stimuli were significantly increased in *Ts*/+ ($n = 12$) compared with +/+ littermate controls ($n = 6$; Fig. 2, *A* and *B*; Table 1). The mean threshold difference at 16 and 32 kHz between +/+ and *Ts*/+ mice did not reach significance levels but the variance differed significantly between the two genotypes ($p < 0.001$; Bartlett's test). Hearing loss at 8 weeks of age affected all test frequencies to a similar degree with an average increase of thresholds of 28 db SPL (Fig. 2*A*; Table 1). After 8 weeks, ABR thresholds at the click, 8, and 16 kHz stimuli stagnated. At these stimuli, there were no significant threshold differences between 8- and 30-week-old and between 30- and 52-week-old *Ts* mice. Hearing thresholds at the 32 kHz, however, differed between 8- and 52-week-old *Ts* mice. However, there was also a significant threshold increase at the 32 kHz stimulus in 52-week-old +/+ animals (Fig. 2*B*). The increase of thresholds in older +/+ mice is presumably the result of the mixed TSJ/LeJ genetic background.

We next measured DPOAEs. In 3-week-old *Ts*/+ mutants ($n = 24$ ears) emissions at the L1 = 75 db SPL stimulus level were significantly reduced over a wide range of test frequen-

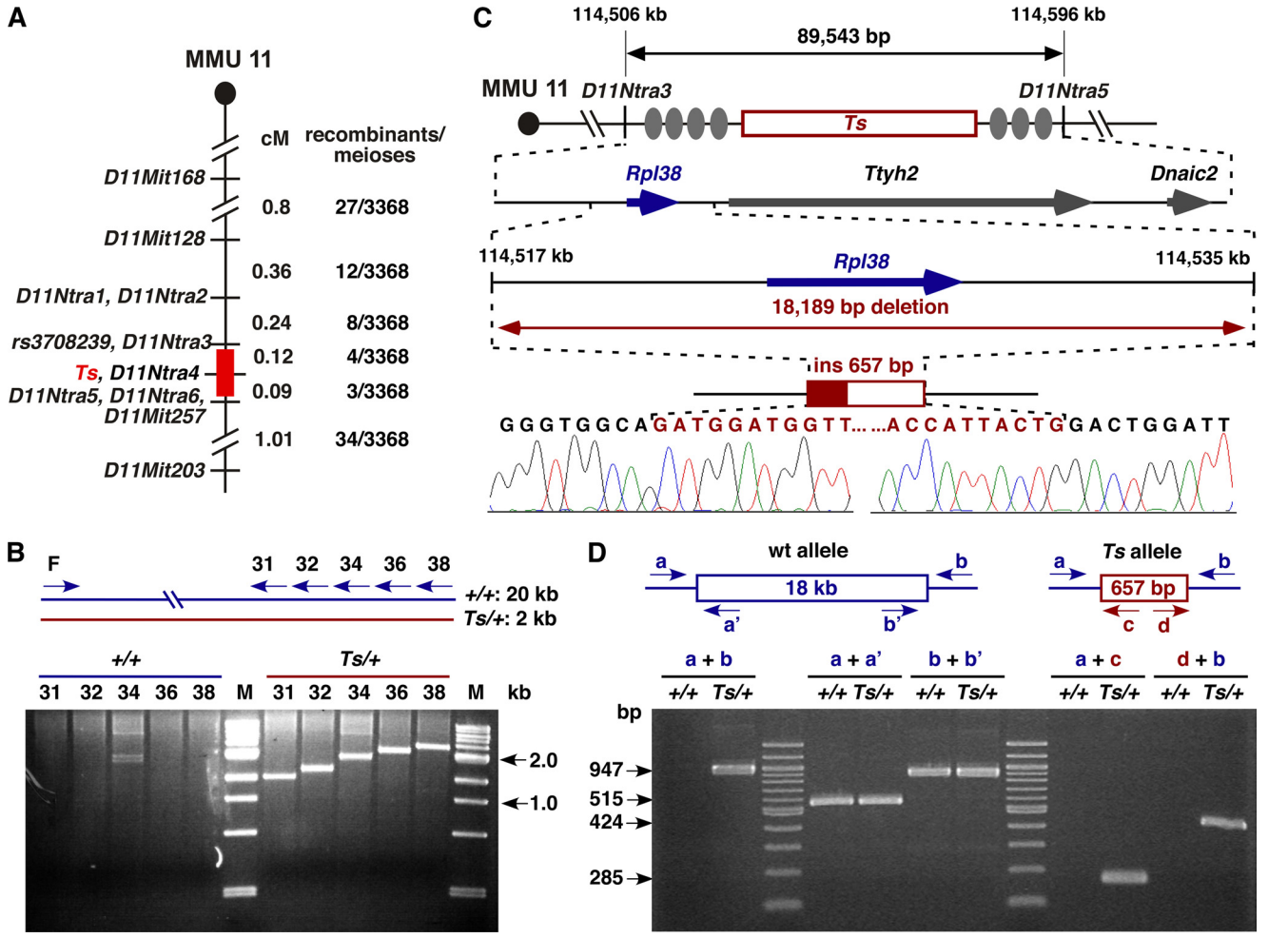

FIGURE 1. **Molecular genetics of *Ts*.** *A,* genetic map of the *Ts* interval on distal MMU 11. Shown is the genetic linkage map obtained from the F2 intercross at the distal portion of mouse chromosome 11 (MMU 11), where locations of genetic markers are shown on the *right*, their genetic distance in centimorgans shown on the *left,* followed by the number of recombinants per meioses that separate each marker. The nonrecombinant critical *Ts* region is shown in *red*. *B,* insertion/deletion PCR screen. A single forward primer (*F*) and five progressively more distal located reverse primers (*R31, -32, -34, -36,* and *-38*) were predicted to produce products ranging from ~19.5 to ~21.0 kb. Instead, products ranging from 1.5 to 3.0 kb were observed exclusively from *Ts*/+ DNA template, indicating the absence of ~18 kb of genomic DNA on the *Ts* chromosome. Shown is a SYBR Green-stained 2% agarose gel separating the amplified products. *Lane M*, DNA size standard. *C,* physical map of the *Ts* critical region. From *top to bottom* is shown the genetic region on chromosome 11 defined by markers *D11Ntra3* and *D11Ntra5* with their physical location given at the *top* in kb. *Filled ovals* represent the approximate locations of recombination events, and the *red box* indicates the location of the *Ts* critical interval. The *arrow* marks the position and orientation of *Rpl38* (ribosomal protein L38), *Ttyh2* (tweety homolog 2), and *Dnaic2* (dynein, axonemal, intermediate chain 2). Sequencing chromatogram of the PCR fragment amplified from the *Ts* chromosome. Bases shaded in *red* represent the insertion sequence. *D,* verification/genotyping PCR scheme. PCR primers flanking the *Ts* mutation (*a* and *b*), within the deleted region (*a'* and *b'*), and within the insertion (*c* and *d*) were generated. All +/+ DNAs tested ($n = 9$) yielded only fragments $a + a'$ and $b + b'$, whereas all *Ts*/+ DNAs tested ($n = 13$) yielded $a + b$, $a + a'$, $b + b'$, $a + c$, and $d + b$.

cies (f2 = 10–50 kHz) compared with 3-week-old +/+ littermate controls ($n = 20$ ears). Emission levels in +/+ ears were slightly reduced compared with normal hearing C3HeB/FeJ mice at 4 weeks of age ($n = 12$ ears), which was most pronounced at the 45–54-kHz frequency range (Fig. 2*C*). Comparison of emission levels at the 16-kHz frequency also showed significant reductions at 65-, 55-, and 45 db SPL stimulus levels between *Ts*/+ and +/+ mice (Fig. 2*D*). Emission levels of *Ts*/+ mice at 12 ($n = 32$ ears) and 48 ($n = 10$ ears) weeks of age were significantly reduced at the 16-kHz frequency being near noise floor levels up to 75 db SPL stimulus level compared with age-matched +/+ littermates ($n = 28$ and $n = 6$ ears, respectively) (Fig. 2*E*). These data suggest that hearing impairment in *Ts* mice starts at around 3 weeks of age and is fully expressed by 8 weeks.

In 20 *Ts*/+ mutants, DPOAE loss occurred in both ears, in nine mutants one ear was affected and in four mice both ears showed emissions greater than 20 db SPL (16 kHz; L1 = 75 db SPL). Penetrance of DPOAE loss in *Ts*/+ ears was 74% ($n = 49/66$; average age, 13 weeks; age range, 3–48 weeks). In age-matched +/+ littermates, five animals showed unilateral hearing loss; none exhibited reduced emission in both ears, and penetrance was 9% ($n = 5/54$; average age, 14 weeks; age range, 3–48 weeks). Despite the reduced penetrance the phenotype/genotype correlation was highly significant ($p < 0.0001$; Fisher's test).

As DPOAEs depend to a large extent on the electrochemical gradient in the endolymph of the scala media, we measured the endocochlear potential. Starting at 4 and up to 48 weeks of age, *Ts*/+ mice had EPs that were in the normal

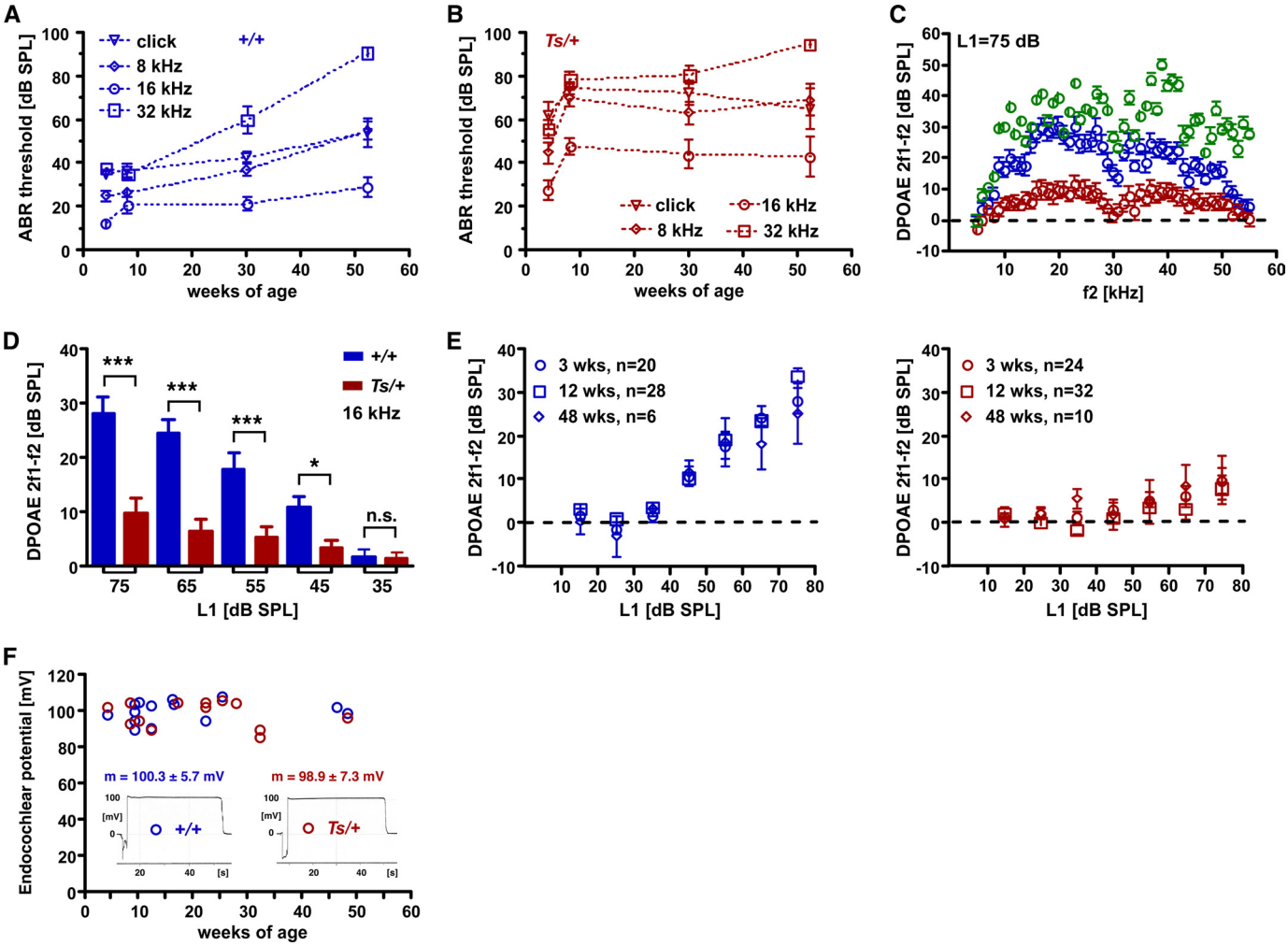

FIGURE 2. **Audiological characteristics of *Ts*.** *A* and *B*, shown are ABR thresholds in db SPL of +/+ (*A*) and *Ts*/+ (*B*) mice at 4, 8, 30, and 52 weeks of age. Thresholds for click (*triangle*), 8 (*diamond*), 16 (*circle*), and 32 kHz (*square*) are given as the mean ± S.D. (see also Table 1). *C*, shown are DPOAE amplitudes at the 2f1 − f2 frequency and L1 = 75 db relative to the noise floor of +/+ (*blue circle*), *Ts*/+ (*red circles*), and C3HeB/FeJ (*green circle*) mice at 3 weeks of age. Mean values ± S.E. of 20 +/+, 24 *Ts*/+, and 12 C3HeB/FeJ ears are plotted. *x* axis shows f2 sweep frequency. *D*, shown are DPOAE amplitudes at the f2 = 16 kHz frequency for input levels (L1) ranging from 35 to 75 db SPL. Mean values ± S.E. of 20 +/+ (*blue bars*) and 24 *Ts*/+ (*red bars*) are shown. ***, $p < 0.001$; *, $p < 0.05$, *n.s.* = not significant. *E*, shown are DPOAE amplitudes at the f2 = 16 kHz frequency for input levels (L1; *x* axis) of +/+ (*left panel*) and *Ts*/+ (*right panel*) at 3 (*circle*), 12 (*square*), and 48 weeks of age (*diamond*). Output level in db SPL relative to noise floor of the 2f1 − f2 frequency (*y* axis) is plotted against input L1 levels (*x* axis). The data are given as mean ± S.E.; *n* = number of ears tested. *F*, given are endocochlear potentials of +/+ (*blue label*) and *Ts*/+ (*red label*) mice at the indicated age (*x* axis). Each *circle* refers to one measurement, and the mean ± S.D. across all ages is given for +/+ and *Ts*/+ mice. Output level in db SPL relative to noise floor of the 2f1-f2 frequency (*y* axis) is plotted against input L1 levels (*x* axis). Values are given in millivolts (*mV*). A representative read-out for each genotype is given as *inset*.

TABLE 1
Hearing thresholds in +/+ and *Ts*/+ mice
Thresholds are given as mean ± S.D. in db SPL; weeks, weeks of age; NS, not significant; *n*, number of animals tested.

Weeks	Genotype	Click	8 kHz	16 kHz	32 kHz	*n*
4	+/+	35 ± 3	25 ± 6	12 ± 3	38 ± 4	6
	Ts/+	62 ± 21	45 ± 17	27 ± 15	56 ± 13	12
	p	<0.01	<0.05	NS	NS	
8	+/+	36 ± 8	26 ± 4	20 ± 9	35 ± 5	6
	Ts/+	74 ± 8	70 ± 12	53 ± 18	78 ± 12	10
	p	<0.001	<0.001	<0.001	<0.001	
30	+/+	42 ± 6	37 ± 8	21 ± 9	60 ± 14	7
	Ts/+	72 ± 22	63 ± 21	44 ± 24	80 ± 17	14
	p	<0.01	<0.05	<0.05	NS	
52	+/+	54 ± 14	55 ± 9	29 ± 10	91 ± 2	5
	Ts/+	65 ± 26	69 ± 19	43 ± 25	95 ± 4	8
	p	NS	NS	NS	NS	

range and did not differ from the EPs of +/+ littermates. The mean EP at the round window averaged over all age groups in *Ts*/+ mice was 98.9 ± 7.3 mV ($n = 13$) and the EP levels in +/+ littermates was 103 ± 6 mV ($n = 14$; $p > 0.05$) (Fig. 2*F*) suggesting a normal stria vascularis function in *Ts*.

Ectopic Ossification and Crystal Deposition in Middle Ear Cavity—Histological and morphological inspection of the *Ts* ear revealed a pathosis in the middle ear. There, the first signs of a phenotype were seen in 3-week-old ears as a locally restricted neo-ossification at the otic capsule. In the normal 4-week-old cochlea, a thin straight bony ridge-like elevation forms at the lateral wall of the otic capsule that reaches into the lumen of the middle ear cavity and extends from the round window up to the apex (Fig. 3, *A* and *B*, *arrows* +/+). This round window ridge is mostly composed of endochondral bone and emerges at the position where the petrous bone of the cochlea adjoins the tympanic bone of the surrounding dorsal bulla (Figs. 3, *A* and *B*, and 4, *E* and *F*). A bony elevation of similar anatomy is present at the side of the oval win-

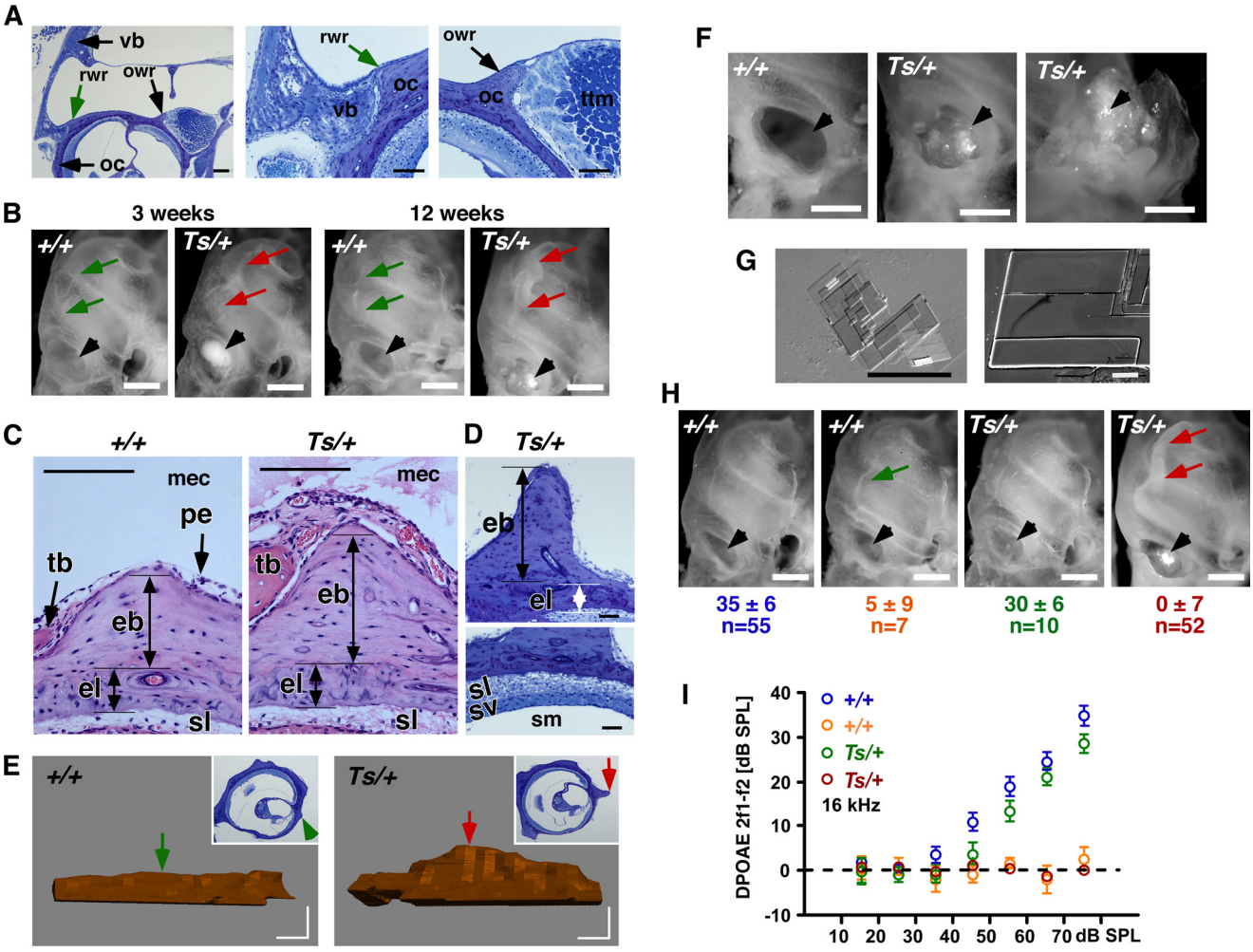

FIGURE 3. **Ectopic ossification and cholesterol crystal deposition in the middle ear.** *A,* images of plastic-embedded toluidine-stained cross-sections through the mouse temporal bone at 4 weeks of age. Bone of the ventral bulla (*vb*, *black arrow*) is indicated. Location of the round window ridge (*arrow*) and oval window ridge (*black arrow*) is indicated; *oc*, otic capsule; *ttm*, tympanic tensor muscle; *scale bar,* 100 μm. *owr*, oval window ridge; *rwr*, round window ridge. *B,* photographs of the cochlea of +/+ and *Ts*/+ mice at 3 and 12 weeks of age are shown. Location of round window ridge in +/+ (*green arrows*) and in *Ts*/+ (*red arrows*) is shown. *Black arrowhead* points to the round window. Note crystal deposition in the round window of *Ts*/+ ears but not in +/+ ears; *scale bar,* 500 μm. *C,* images of paraffin-embedded hematoxylin and eosin-stained cross-sections through the round window ridge in +/+ and *Ts*/+ ears at 12 weeks of age. *vb*, ventral bulla; *pe*, periosteum; *eb*, endochondral bone; *el*, endosteal layer; *sl,* spiral ligament; *mec*, middle ear cavity; *tb*, tympanic part of temporal bone; *scale bar,* 100 μm. *D,* images of plastic-embedded toluidine-stained cross-sections through the round window ridge of a *Ts*/+ ear at 11 weeks of age (*nøbben*). *sv*, stria vascularis; *sl*, spiral ligament; *sm*, scala media; *eb*, endochondral bone; *el,* endosteal layer; *scale bar,* 50 μm. *E,* three-dimensional reconstruction of the round window ridge in +/+ (*left*) and *Ts*/+ (*right*) mice at 11 weeks of age. *Inset* shows a representative cross-section used for the reconstruction. *Arrow* points to the corresponding location of the round window ridge in the section and three-dimensional model; *scale bar,* 50 μm. *F,* photographs of the round (*left* and *middle panel*) and oval (*right panel*) window in +/+ (*left panel*) and *Ts*/+ (*middle* and *right panel*). Note the excessive crystal deposition at the round (*middle*) and around the ossicles at the oval (*right*) window (*arrow head*); *scale bar,* 500 μm. *G,* bright field (*left*) and scanning electron microscope (*right*) image of crystal deposits isolated from the round window of *Ts*/+ ears; *scale bar,* 100 and 50 μm. *H,* photographs of cochlea of +/+ and *Ts*/+ mice showing crystal deposition at the round window (*black arrowhead*) and *nøbben* formation (*red arrow*) as function of DPOAE levels. Emission levels are given in db SPL at f2 = 16 kHz input frequency and L1 = 75 db SPL input level. Mean ± S.D. are given for number (*n*) of ears tested. Note the normal round window ridge and no crystal deposition in *Ts*/+ ears with normal DPOAEs; *scale bar,* 500 μm. *I,* input/output function of DPOAEs at f2 = 16 kHz of +/+ ($n = 62$) and *Ts*/+ ($n = 62$) ears showing two discrete classes of phenotypes in each genotype. Average age of +/+ mice was 16 weeks (range: 3–48) and *Ts*/+ mice was 17 weeks (range, 3–48). Output levels in db SPL relative to noise floor on *y* axis, and L1 input levels at the *x* axis. Symbols represent mean ± S.E.

dow. This oval window ridge forms the lateral side of a groove that harbors the tympanic tensor muscle (Fig. 3*A*). In *Ts* cochleae, neo-ossification of the round window ridge (here named "*nøbben*"; Norwegian for outcropping) was detected 3 weeks after birth ($n = 12$ ears) and became fully expressed by 12 weeks of age ($n = 26$ ears; Fig. 3*B*; *arrows Ts*/+). Histological cross-sections revealed the massive formation of endochondral bone extending into the middle ear cavity that occasionally reached a height of ~300 μm, compared with the height of a normal round window ridge of ~150 μm ($n = 12$ ears; Fig. 3, *C* and *D*, *Ts*/+). Three-dimensional reconstructions of one representative ear using serial sections that covered a length of 350 μm revealed a 1.5-fold increase in the volume of the ectopic endochondral bone in *Ts*/+ compared with the normal round window ridge of a +/+ ear (Fig. 3*E*). The endosteal layer of the otic capsule was of normal thickness in *Ts*, and the *nøbben* had no adverse effect on the morphology of the underlying cellular layers (*i.e.* spiral fibrocytes and stria vascularis of the inner ear) (Fig. 3, *C* and *D*). Along with this, we observed excess deposition of fine crystals in the

TABLE 2

Penetrance of DPOAE levels and ectopic mineralization in *Ts* mice

Number of ears that express (+) or do not express (−) the trait. %, penetrance; *p*, Fisher's test.

	DPOAE			Ossification				Crystals			
	+	−	%	+	−	%	*p*	+	−	%	*p*
+/+	55	7	11	1	61	2		0	62	0	
Ts/+	10	52	84	54	8	87	<0.0001	52	10	84	<0.0001

middle ear. In 3-week-old *Ts* cochleae ($n = 12$ ears), large aggregates of crystals were seen within the round window and at the oval window. The crystals surrounded, and in some ears, completely covered the stapes (Figs. 3*F*, also *B* and *H*, *arrowhead*). Frequently, a sea of crystals filled the entire cavity. Using bright field and scanning electron microscopy, the crystals differed in size and had a flat and thin appearance (Fig. 3*G*). Both the bone and crystal formation varied in their penetrance and expressivity. In a total of 62 *Ts*/+ ears (average age, 17 weeks; age range, 3–48 weeks), penetrance of ossification and crystal formation was 87 and 84%, respectively. In this population, penetrance of DPOAE loss was 84% and significantly correlated with the ectopic ossification ($p < 0.0001$) and crystal formation ($p < 0.0001$) (Fig. 3, *H* and *I*, and Table 2). Similarly, the association between *nøbben* ($n = 54$) and crystal formation ($n = 52$) was significant ($p < 0.0001$).

No other gross morphological defects were readily detected in the ears of *Ts* mice. Most notably, the middle ear bones exhibited a normal morphology, although some signs of cellular debris deposition could be seen on *Ts* stapes. Cross-sections of the cochlear duct of 8-week-old *Ts*/+ mutants ($n = 5$) revealed a normal appearance of the organ of Corti, the stria vascularis, and the spiral ganglion compared with age-matched +/+ littermate control cochleae ($n = 4$). Furthermore, the cellular pattern and hair cell planar polarity of the organ of Corti were unaltered in *Ts* (supplemental Fig. S2).

Chronic Inflammation with Effusion in Ts—The abnormal mineralization of the middle ear cavity was accompanied by a chronic inflammation with effusion. In the normal otic capsule, the periosteum forms a thin cellular layer, consisting of osteoblasts, collagen fibers, and fibroblasts, that covers the outer layer of the bony cochlea. In *Ts* ears, starting at 2 weeks of age, the periosteal layer appeared dilated, swollen, and delaminated from the underlying bone (Fig. 4, *A* and *B*). At 3 weeks, the dilation and outward growth of the periosteum became more pronounced. In addition, we noticed the appearance of cellular debris-like aggregates in the middle (Fig. 4*C*) and apical region (Fig. 4*D*) of the middle ear cavity. In 12-week-old *Ts*/+ ears ($n = 12$), the inflammation had progressed to a chronic inflammation with effusion, as evidenced by the eosinophilic serous exudate (pus) in the middle ear cavity (Fig. 4, *E* and *F*) and the abundance of cellular aggregates and debris containing cells typical of the monocyte-macrophage lineage (Fig. 4, *G–J*).

The space around the stapedial footplate at the oval window was filled with exudate, but the annular stapedial ligament, which connects the footplate with the oval window and is often the site of otosclerotic plaque formations, was normal in *Ts* (Fig. 4*K*). Furthermore, the round window membrane was normal despite massive concentration of minerals, serofibrinous precipitates, and cellular debris in the round window (Fig. 4, *L* and *M*). We did not observe exudate or cellular infiltrates in the endo- and perilymph of the inner ear (Fig. 4*F*).

In 36-week-old *Ts*/+ ears ($n = 2$), the inflammation persisted as seen by the dilated and delaminating periosteum (Fig. 4, *N–P*) and the cellular debris around the round window (Fig. 4*Q*). In the middle ear cavity near the round and oval window, there were also large aggregates of condensed mineralized extracellular debris, with some interspersed macrophages (Fig. 4, *R* and *S*). We furthermore observed node-like cell masses near the round window membrane and attached to the cochlear wall. These nodes contained fibroblasts and macrophages and presented with randomly oriented spindle-shaped cholesterol clefts (Fig. 4, *T* and *U*).

In a sample of five 56-week-old *Ts*/+ mice, we found eight ears with pus and crystal deposition in the middle ear and around the stapes. In some instances the debris around the stapes had a red-like appearance indicative of hemorrhage (Fig. 4, *V* and *W*). Together, these data suggest that the inflammation is chronic and persists throughout life.

To ascertain the microbial status, sterile aliquots of the middle ear fluid were obtained and cultured on agar plates for 48 h. Eight out of 16 *Ts*/+ ears of 4-, 16-, and 52-week-old mutants showed sporadic growth of bacteria, which were typed as *Staphylococcus warneri*, *Staphylococcus xylosus*, *Staphylococcus epidermidis*, and *Enterococcus faecalis*. However, 4 out of 10 +/+ littermate control ears showed similar growth characteristics and bacterial type. In two 52-week-old middle ears that were filled with fluid and pus, no bacteria could be isolated. There was no clear correlation between the presence of pus and bacterial growth. Only 8 out of 13 ears with pus showed bacterial growth. Perforation of the tympanic membrane, a hallmark of suppurative chronic otitis media, was not observed.

Enlarged Eustachian Tube in Ts—Middle ear inflammation is often found in connection with craniofacial deformities that affect the shape of the Eustachian tube. Serial cross-sections through the ventral tip of the middle ear revealed the Eustachian tube at the anterior wall of the middle ear as a hollow narrow opening surrounded by the cartilaginous segment (Fig. 5*A*). In ears at 3, 4, 12, and 36 weeks of age ($n = 5$ ears), we noted a wider opening of the ET in *Ts*/+ compared with their +/+ controls ($n = 4$). In mutant ears the opening was round and wide, whereas in +/+ controls it appeared stretched and tight. The cross-sectional area at the opening was on average 1.6 times larger in *Ts*/+ than in +/+ ears. In one representative +/+ ear at 3 weeks of age, the perimeter of the Eustachian

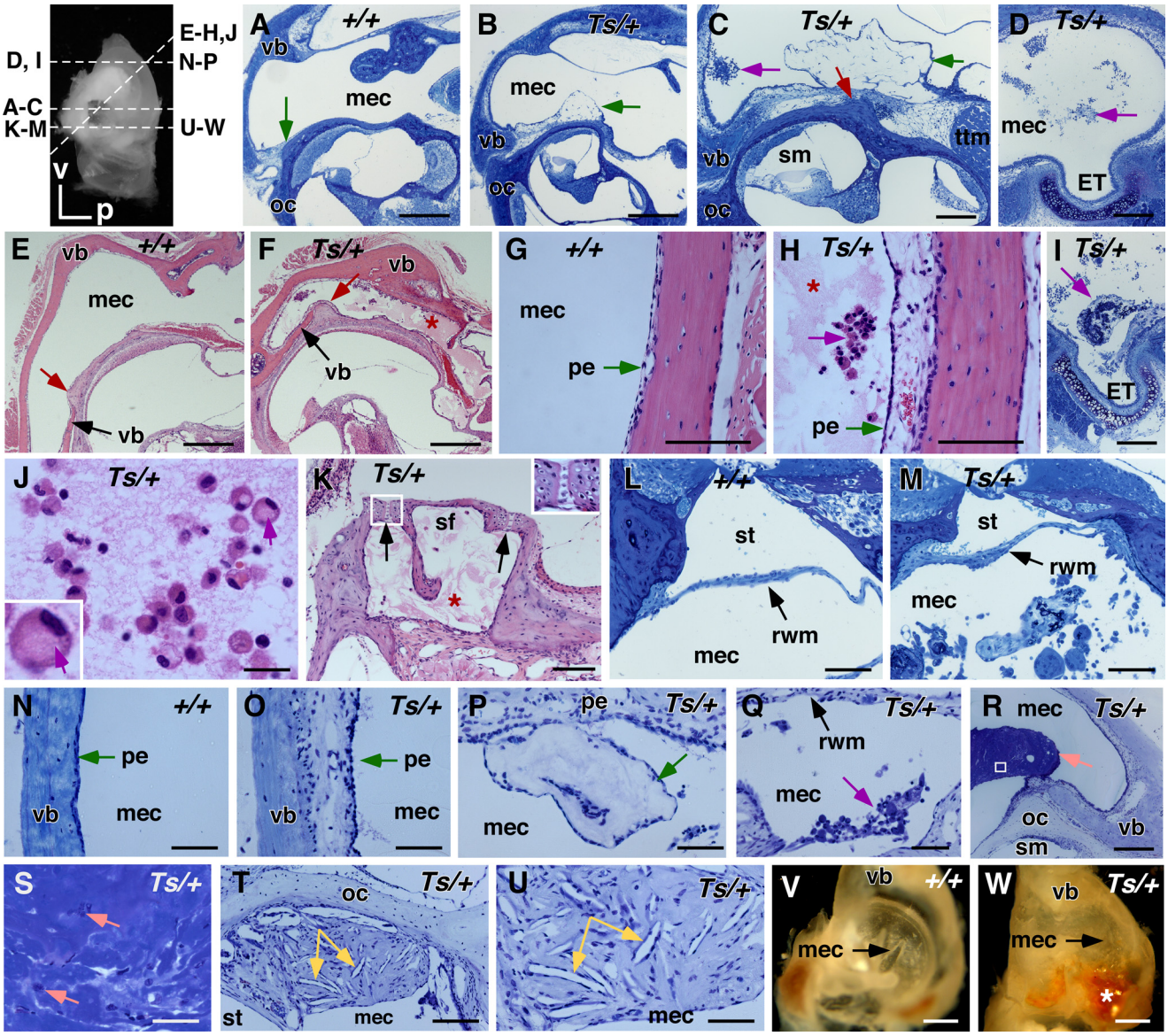

FIGURE 4. **Inflammation of the middle ear cavity.** *Inset, top left,* shows the mouse ear indicating the plane of the section (*dashed line*) corresponding with the figure (*A–W*); *v,* ventral; *p,* posterior. *A–D,* images of plastic-embedded toluidine-stained cross-sections of 2-week-old +/+ (*A*) and *Ts*/+ (*B*) and 3-week-old *Ts*/+ (*C* and *D*) ears; *green arrow*, periosteum; *pink arrow*, cellular debris; *red arrow*, *nøbben*; *scale bar* (*A* and *B*) 400 μm; *C* and *D,* 200 μm. *E–H,* images of paraffin-embedded hematoxylin and eosin-stained cross-sections of 12-week-old +/+ (*E* and *G*) and *Ts*/+ (*F* and *H*) ears; *red arrow*, round window ridge; *pink arrow*, cellular debris; *red star*, exudate; *scale bar* (*E* and *F*) 400 μm; *G* and *H,* 100 μm. *I,* image of plastic-embedded toluidine-stained cross-section of 12-week-old *Ts*/+; *red arrow* points to cellular debris and fibrinous aggregates at the opening of the Eustachian tube; *scale bar,* 200 μm. *J,* image of paraffin-embedded hematoxylin and eosin-stained cross-section of 12-week-old *Ts*/+ showing high magnification of *H* of cellular aggregates and eosinophilic exudates in the middle ear; *green arrow* points to a macrophage with vacuolated cytoplasm (also *inset, left bottom*); *scale bar,* 20 μm. *K,* image of paraffin-embedded hematoxylin and eosin-stained cross-section of 12-week-old *Ts*/+ showing middle ear space around the stapedial footplate (*sf*); *red star*, eosinophilic exudate; *black arrow* points to the annular stapedial ligaments; *white box* shows enlarged annular stapedial ligament; *scale bar,* 100 μm. *L* and *M*. images of plastic-embedded toluidine-stained cross-sections of 12-week-old +/+ (*L*) and *Ts*/+ (*M*) showing the middle ear at the round window; *arrows* point to the round window membrane (*rwm*). Also, note the cellular aggregates and fibrinous precipitate in the middle ear cavity (*mec*), but not in the scala tympani (*st*); *scale bar,* 100 μm. *N–U,* shown are images of plastic-embedded toluidine-stained cross-sections of 36-week-old +/+ (*N*) and 36-week-old *Ts*/+ (*O–U*) ears. Note the dilated (*O*) and delaminated (*P*) periosteum along the ventral bulla and the cell debris at the round window membrane. Also shown is a mineral aggregate (*R; arrow*) over the round window ridge and a magnification in *S* with *arrows* pointing to macrophages. *T* shows a cholesterol granuloma in the middle ear cavity located at the otic capsule and the round window membrane. *Yellow arrows* in *T* and *U* point to cholesterol clefts; *scale bar, R*, 200 μm; *T*, 100 μm; *N–Q* and *U*, 50 μm; *S,* 40 μm. *V* and *W,* shown are photographs of the inside of the ventral bulla of a 78-week-old +/+ (*V*) and 56-week-old *Ts*/+ (*W*) ear. Note the pus (*black arrow*) and crystals with signs of hemorrhage (*white star*) in the *Ts* specimen; *scale bar,* 1 mm. *mec*, middle ear cavity; *vb*, ventral bulla; *oc*, otic capsule; *ttm*, tympanic tensor muscle; *ET,* Eustachian tube; *sm*, scala media; *pe*, periosteum; *sf*, stapedial foot plate; *st*, scala tympani; *rwm*, round window membrane.

tube at the opening measured 1338 ± 38 μm ($n = 5$ sections), and the cross-sectional area of the lumen measured 87,441 ± 10,234 μm^2 (Fig. 5, *A* and *C*). In the 3-week-old *Ts*/+ ear, the Eustachian tube at the opening was significantly larger with a perimeter of 1564 ± 70 μm and the cross-sectional area of 162,789 ± 13,943 μm^2 ($n = 5$ sections; $p < 0.001$) (Fig. 5, *B* and *D*). Three-dimensional reconstruction of serial sections of the lateral portion of the Eustachian tube revealed a 2.8-fold increase in volume in the 3-week-old *Ts* ear compared with the +/+ control (Fig. 5, *A* and *B*).

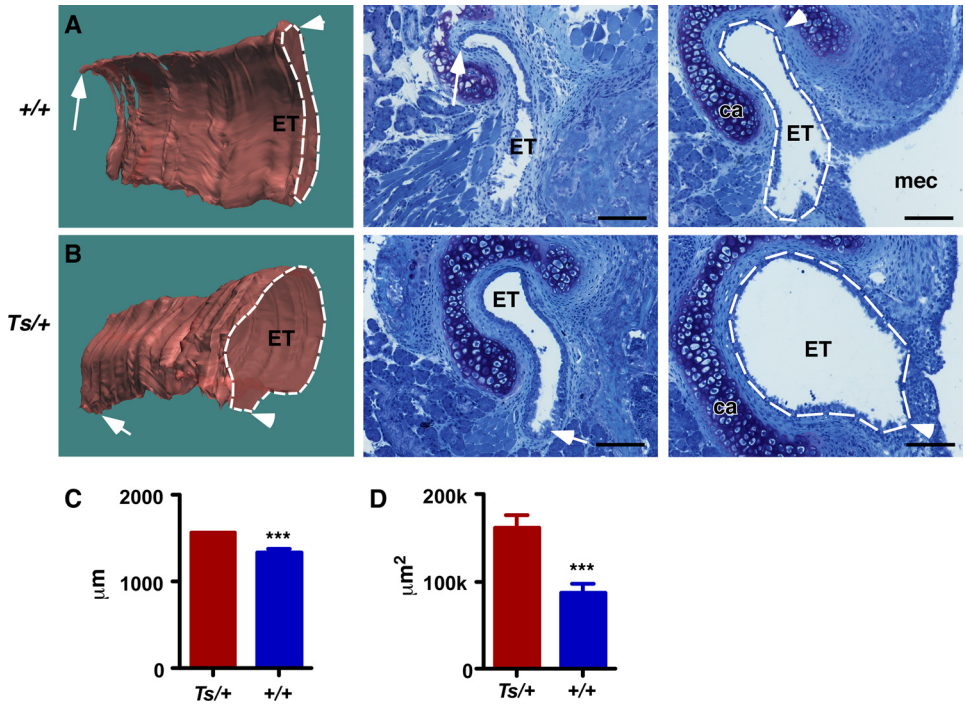

FIGURE 5. **Enlarged Eustachian tube in *Ts*.** *A* and *B*, three-dimensional reconstructions of the Eustachian tube of a 3-week-old +/+ (*A*) and *Ts*/+ (*B*) ear based on serial sections. Representative sections are shown in the *middle* and *right panel*. The lumen of the Eustachian tube is outlined by the *white lines*. Orientation and location of sections on the respective three-dimensional model are shown as *arrow* and *arrowhead*. *MEC*, middle ear cavity; *ET*, Eustachian tube; *ca*, cartilaginous tissue; *m*, medial; *d*, dorsal. *Scale bar*, 50 μm. Volume of ET in *Ts*/+ measured 50,489,630 μm^3 and in +/+, it was 17,418,522 μm^3. *C* and *D*, graphs showing perimeter (*B*) and cross-sectional area (*D*) of ET in *Ts*/+ and +/+; $n = 5$ serial sections. ***, $p < 0.001$.

Aside from the ear phenotype, a comprehensive phenotypic analysis revealed abnormally shaped tails and shortened noses. Among a series of serological markers, organic phosphate was significantly elevated in *Ts* with a mean of 8.2 ± 1.23 mg/dl compared with 6.6 ± 0.85 mg/dl in +/+ littermates ($p = 0.028$; $n = 6$). Body weight was reduced in 8-week-old *Ts* with a mean of 20 ± 3 g ($n = 17$) compared with 24 ± 3 g in +/+ mice ($n = 26$; $p < 0.001$). The cellular hematology was normal (supplemental Table S1).

Rpl38 Expression and Localization in Cochlea and Erythrocytes—To determine the function of Rpl38 in the ear, we generated polyclonal antisera Pb863 and Pb865. To ascertain their specificity, we probed protein lysates of HEK293T cells transfected with Myc-tagged Rpl38. On Western blots, both affinity-purified antisera recognized a distinct band of ~8 kDa in the transfected but not in the untransfected lysate. The same ~8-kDa band was also detected with the anti-Myc antibody (Fig. 6*A*). On protein extract of +/+ and *Ts*/+ ears, Pb865 recognized an ~8-kDa protein species with equal intensity in both lysates. Likewise, the Rpl38 antibody showed strong reactivity with protein lysates prepared from whole blood cells (Fig. 6*B*). Quantitation of staining intensities, controlled for equal amounts of peripheral blood cell numbers, protein concentration, and anti-actin staining, showed equal amounts of Rpl38 being present in +/+ and *Ts*/+ whole blood cells (data not shown). Preincubation of Pb865 with excess of the synthetic peptide used to generate the antibody, effectively blocked the appearance of the ~8-kDa band in ear and blood protein extracts. In addition, the peptide also blocked the binding of the higher molecular weight bands observed in the ear protein lysate (Fig. 6*C*). The higher molecular weight bands in the ear lysate may represent native complexes containing Rpl38 or incompletely solubilized Rpl38 protein aggregates.

To determine the tissue distribution, we stained inner and middle ear tissues with Pb865. In whole mount preparations of the organ of Corti and the stria vascularis at postnatal day 5, we found clear and strong staining of red blood cells in the vas spirale (the blood vessel underlying the organ of Corti) and in the vasculature of the stria vascularis (Fig. 6, *D–F*). In cryosections of adult cochlear tissue, we found abundant staining of blood cells in the vas spirale (Fig. 6*G*) and in other blood vessels of the membranous labyrinth such as in the stria vascularis (Fig. 6*H*) and the spiral limbus (data not shown). In cryosections of adult middle ear, staining of blood cells located within the periosteal membrane and within the vasculature of the bony labyrinth was readily detected (Fig. 6*I*). There was no difference in the staining between +/+ and *Ts*/+ ear tissue (data not shown), and no other regions in the middle and inner ear showed specific staining. On adult blood spreads, staining was most pronounced for mature non-nucleated erythrocytes and was concentrated around the plasma membrane. No difference between +/+ and *Ts*/+ blood spreads were noted (Fig. 6, *J* and *K*) and staining with a nonspecific rabbit IgG antibody did not produce any discernible signal (Fig. 6*M*). In addition, the Pb865 staining in the stria vascularis and erythrocytes was efficiently blocked by the synthetic peptide specific for the Pb865 epitope (Fig. 6, *M* and *N*).

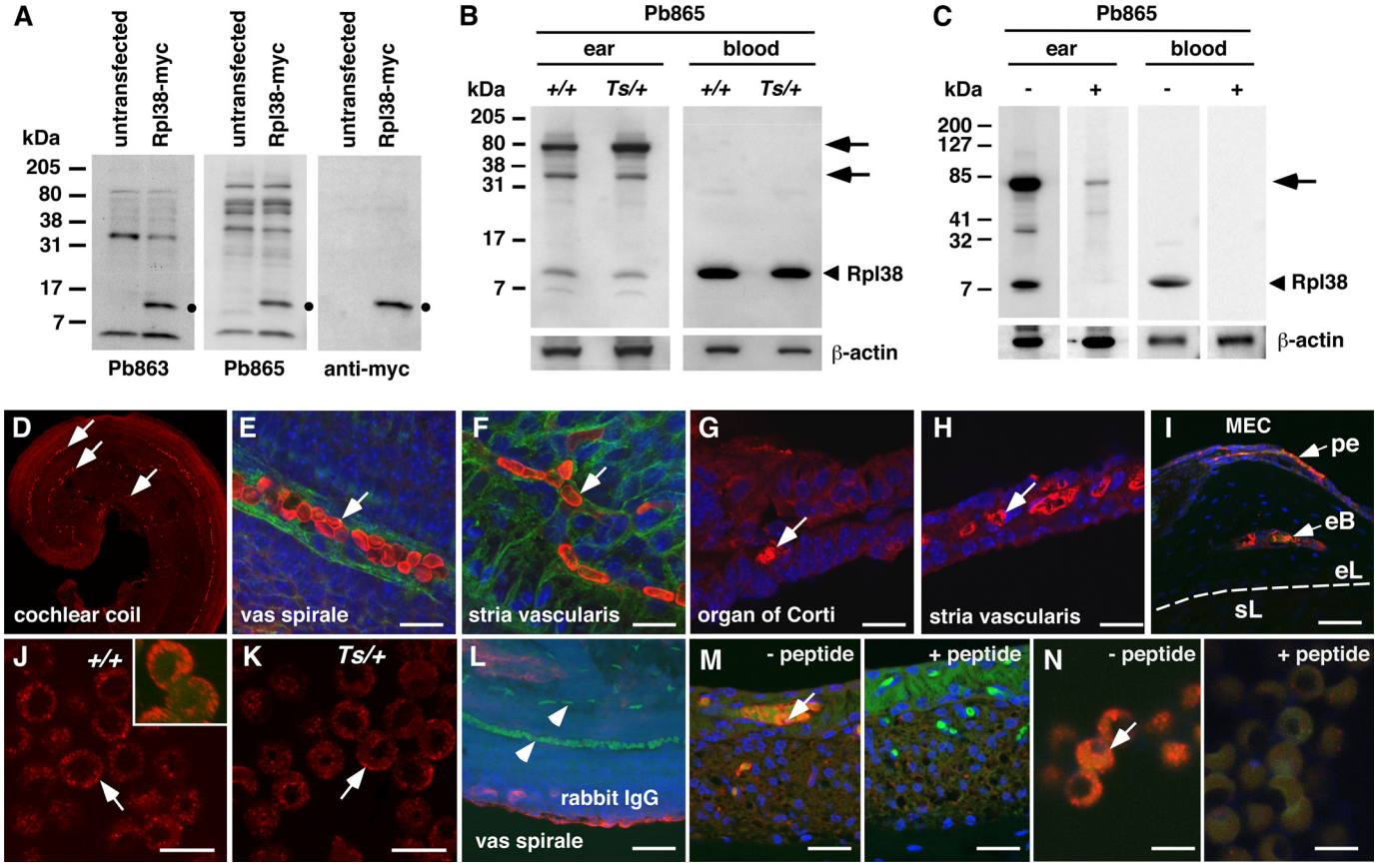

FIGURE 6. **Tissue expression and immunolocalization of Rpl38.** *A–C,* Western blots of protein extracts from HEK293T cells (*A*) and tissue extracts of adult +/+ and *Ts*/+ mice (*B*) in the presence (+) and absence (−) of Pb863-specific peptide (*C*). *Left side* of each panel indicates the molecular mass in kDa. *A,* membranes stained with Pb863, Pb865, and anti-Myc antibody of HEK293T cells transfected and nontransfected with a mouse RPL38-myc fusion construct. *Black dot* indicates Rpl38-specific band present in the transfected but not in untransfected lysate. *B,* Western blot of protein extract from the ear and blood of +/+ and *Ts*/+ mice blotted with Pb865 and β-actin antibody. *Arrowhead* indicates the ~8-kDa Rpl38 protein band. *Arrows* point to higher molecular weight bands in ear lysate. Protein lysates were also hybridized with β-actin antibody to control for equal loading. *C,* ear and blood protein lysates were incubated with Pb865 in the presence (+) and (−) absence of Pb865-specific peptide. Note that both the ~8-kDa and higher molecular weight protein species are effectively blocked by the peptide. Membranes were hybridized with β-actin antibody to control for equal transfer efficiency. *D--N,* shown are confocal images of cochlear coil (*D* and *E*) and stria vascularis (*F*) whole mount preparations, cryosections of organ of Corti (*G*), stria vascularis (*H*), otic capsule (*I*), and blood spreads (*J* and *K*) stained with the Pb865 antibody (*red channel*). *E–I* and *L--N,* counterstained with DAPI (*blue channel*); *E* and *F,* counterstained with phalloidin (*green channel*); *L,* staining with nonspecific rabbit IgG antibody. *J, inset* shows high magnification of Z-stack of Rpl38-positive erythrocyte showing staining near the plasma membrane. *White arrows* (*D–N*) point to Rpl38-positive staining, and *arrowhead* in *L* points to nonstaining erythrocytes. *M* and *N,* staining of stria vascularis (*M*) and blood spread (*N*) with Pb865 in the absence (−) and presence (+) of Pb865-specific peptide. Note that Pb865 staining is blocked in the presence of competing peptide. *pe*, periosteum; *eb*, endochondral bone; *el*, endosteal layer; *sl*, spiral ligament; *MEC,* middle ear cavity. *Scale bars, E* and *F*, 10 μm; *G* and *H*, 20 μm; *I*, 50 μm; *J, K* and *N*, 5 μm; *L* and *M*, 20 μm.

Rpl38 cDNA Transgene Rescues the Ts Phenotype—The *Ts* mutation may have eliminated or introduced regulatory sequences not associated with Rpl38 function. To prove that the skeletal and hearing phenotypes were directly caused by the deletion, we generated a transgenic mouse line expressing *Rpl38* cDNA under the control of the ubiquitous mouse ROSA26 promoter. In the N1 and subsequent N2 and F2 generations, *Ts*/+ mice carrying the transgene (*Ts*/+ tg+, $n = 15$) had a normal tail, whereas *Ts*/+ mice without the transgene (*Ts*/+ tg-, $n = 11$) exhibited the skeletal phenotype typical of *Ts* mice ($p < 0.0001$, Fig. 7*A* and Table 3). No *Ts*/+ tg+ animal with a Tail-short phenotype was observed. Interestingly, all offspring of the N1 generation regardless of their genotype at *Ts* had normal hearing, based upon their normal DPOAEs. However, in the F2 and N2 generations, the input/output function at f2 = 16 kHz and L1 = 55 db SPL of *Ts*/+ *tg*− ears ($n = 12$) showed significantly reduced emissions compared with +/+ tg+/− ears ($n = 62$). Interestingly, *Ts*/+ tg+ ears showed significantly higher emission levels compared with *Ts*/+ tg− ears ($p < 0.001$) (Fig. 7*B* and Table 3). Using ABR, we found that hearing thresholds were significantly lower in *Ts*/+ tg+ mice ($n = 7$) than in *Ts*/+ tg− mice ($n = 6$; $p < 0.01$). In addition, hearing thresholds in *Ts*/+ tg+ were not different from those of normal hearing +/+ tg+/− mice ($n = 13$; $p > 0.05$) (Fig. 7*C* and Table 3). DPOAE levels and ABR thresholds in *Ts*/+ tg+, *Ts*/+ tg−, and +/+ tg+/− mice slightly differ from those of *Ts*/+ mice of the isogenic TSJ/LeJ strain (Fig. 2, *A* and *D*). We attribute this better hearing to the mixed TSJ.FVB genetic background. Furthermore, whereas *Ts*/+ tg− ears ($n = 6$) demonstrated crystal deposition, ossification, and hemolysis, transgenic *Ts* (*Ts*/+ tg+; $n = 8$) and wild type (+/+ tg(+/−); $n = 20$) ears showed no signs of a middle ear pathology. Together, the data suggest that expression of *Rpl38* on *Ts*/+ mutants rescued the skeletal and hearing phenotypes.

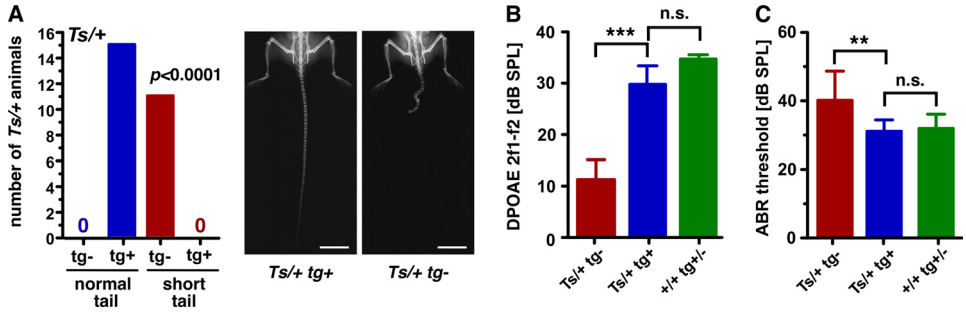

FIGURE 7. **Transgenic rescue of *Rpl38* deficiency.** *A,* number of mice with a *Ts/+* genotype as function of normal and short tail in the presence (+) or absence (−) of the transgene (*tg*). *Right panel* shows representative x-ray photographs of the tail morphology in transgene-positive (*left*) and transgene-negative (*right*) *Ts/+* animal; *scale bar,* 1 cm. *B,* DPOAE emission levels in db SPL relative to noise floor of the 2f1 − f2 frequency at f2 = 16 kHz and L1 = 55 db SPL input; *bars* are mean ± S.E.; ***, $p < 0.001$; *n.s.* = not significant. *C,* ABR thresholds in db SPL at click stimulus; *bars* are mean ± S.D.; **, $p < 0.01$; *n.s.* = not significant.

TABLE 3

Skeletal and auditory phenotypes in *Rpl38* transgenic *Ts* mice

Number of tails and ears that express the indicated phenotype are given as mean ± S.D. *p*, ANOVA test. *Ts*, Tail-short; tg, transgene.

	+/+ tg+/−	Ts/+ tg+	Ts/+ tg-	p
Skeletal				
Normal tail	41	15	0	<0.0001
Short tail	0	0	11	
DPOAE				
16 kHz	35 ± 7 $n = 64$	30 ± 15 $n = 16$	11 ± 14 $n = 12$	<0.001
ABR				
Click	32 ± 4 $n = 22$	31 ± 4 $n = 7$	40 ± 9 $n = 6$	<0.01

DISCUSSION

In this study we found that the *Ts* phenotypes are caused by a large scale deletion of the *Rpl38* gene. The mutation leads to ectopic ossification and cholesterol crystal deposition in the middle ear cavity, an enlarged Eustachian tube, and chronic inflammation with effusion that together result in a conductive hearing loss starting at around 3 weeks of age.

We provide compelling evidence that the deletion of *Rpl38* in the heterozygous state causes the *Ts* phenotypes. This is based on a high resolution genetic map, exon sequencing of the three genes in the critical interval, perfect skeletal phenotype/genotype correlation, and the rescue of the skeletal and auditory defects by an *Rpl38*-expressing transgene. Deficiency of ribosomal proteins is known to underlie *Ts*-like phenotypes in *Drosophila*, mouse, and human. In *Drosophila melanogaster*, a class of more than 50 mutants, called *minutes,* are homozygous lethal, and heterozygotes weigh less and are less viable, all of which are hallmarks of *Ts* (36). *minute* mutants with characterized mutations are haploinsufficient for a riboprotein gene, and the phenotypes are attributed to reduced rates of cell proliferation caused by a reduction in the maximal rate of protein synthesis (37). In humans, haploinsufficient mutations in *RPS10, RPS19, RPS24, RPS26, RPL5,* and *RPL11* underlie a condition known as Diamond-Blackfan anemia, which also often includes mild craniofacial and skeletal abnormalities (38–43). Recently, a screen of ribosomal genes in a large cohort of individuals with Diamond-Blackfan anemia for mutations did not reveal a mutation in *RPL38* (39). In addition, our own screen of a large patient group with autosomal recessive hearing loss did not uncover a mutation,[3] suggesting that *Rpl38* deficiency in humans may be embryonic lethal or manifests in a different pathological context.

Rpl38 is predominantly and abundantly expressed in erythrocytes. This observation does not exclude low level expression in other cell types as one would expect for a ribosomal protein, but rather it points to an extra-ribosomal function (44). A function for Rpl38 during erythropoiesis is suggested by the anemia that is observed in *Ts* embryos as early as E9.0 (29). It is interesting to note that ~30% of heterozygotes die during the perinatal period, which coincides with the transition of erythropoiesis from the liver to the bone marrow (45). Interestingly, adult heterozygotes have normal levels of red blood cells, hemoglobin, hematocrit, and mean corpuscular volume (supplemental Table S1) (28, 29). Also, osmotic fragility tests and cochlear blood flow measurements by laser Doppler flowmetry showed normal erythrocyte function in *Ts* mice.[4] Furthermore, quantitative comparison of Rpl38 protein levels between *Ts/+* and +/+ adult whole blood did not reveal any significant differences. In addition, *Rpl38* mRNA levels were not different between *Ts/+* and +/+ in 2-week-old cochleae (supplemental Fig. S3). The apparent lack of a gene dosage effect in postnatal and adult *Ts* tissue may be due to compensation at the transcriptional level. A similar normalization effect of *Rps19* mRNA expression was recently shown in $Rps19^{+/-}$ mice (46). Together, these observations suggest that a major effect of the *Rpl38* deletion is realized as anemia during the embryonic development, which is overcome in the adult. The ~70% of *Ts/+* heterozygotes that survive the embryonic anemia have a normal life span and show very few pathological features except for their hearing loss. Interestingly, it appears that the middle ear phenotype is susceptible to stochastic factors and genetic backgrounds. The middle ear pathology is only ~80% penetrant and TSJ.FVB-*Ts/+* F1 (see above) and TSJ.BlackSwiss-*Ts/+* F1 hybrids[4] have normal hearing, although they do exhibit the skeletal defects. The effect of the genetic background is also seen by the elevated hearing thresholds in 52-week-old +/+ and *Ts/+*, which is presumably due the presence of the $Cdh23^{ahl}$ allele (47). However, the precise role of the *Rpl38* deletion during erythropoiesis, in adult erythrocytes, and its implication in the middle ear phenotypes remain to be determined.

[3] R. Smith, M. Hildebrand, and K. Noben-Trauth, unpublished observations.

[4] K. Noben-Trauth and H. Neely, unpublished observations.

As extra-ribosomal functions for ribosomal proteins have been suggested in the past (48), the ribosome-free erythrocyte provides an excellent biochemical system to study such a function for Rpl38.

The concomitant manifestation of the *nøbben*, cholesterol crystals, widened Eustachian tube, and inflammation currently prevents the establishment of a clear chain of events. However, there is some room for speculations. Neo-ossification of the cochlear bone is also a hallmark of labyrinthitis ossificans (8) and the Palmerston North autoimmune mouse strain (49). In labyrinthitis ossificans, the bone is the late stage result of an acute bacterial meningitis and inflammation. The ectopic bone is formed by osteoblasts (osteoblastic type) as found in human temporal bones (50) or may result from deposition of calcium salts (calcospherite) by fibroblasts as described in the gerbil model (51). In both cases, the ectopic bone occurs as an outgrowth of the endosteal layer, without affecting the structure of the endochondral bone. In the Palmerston North mouse, the neo-ossification is due to abnormal mineralization of connective tissue triggered by hypertrophic fibroblasts next to the bone of the modiolus (49). Neo-ossification on the outside of the cochlear wall was also described in the LP/J strain. There, deposition of new bone occurred immediately apical to the round window, around the stapedial artery, and at the apex (24). However, in *Ts,* formation of new bone is only seen on the outside of the cochlear wall and is restricted to the round window ridge. The cause of this bone deposition is unclear but may involve the activation of osteoblasts or fibroblasts at the prospective round window ridge. It is interesting to note that osteoblasts were recently shown to form part of the hematopoietic stem cell niche (52), and it is tempting to speculate that the same molecular events that affect erythropoiesis may also sensitize osteoblasts. The initial trigger may come from the increased organic phosphate levels as measured in *Ts* serum (53). This activation may be most pronounced at the round window ridge, where the petrous and tympanic temporal bones form a contact point. The involvement of the tympanic temporal bone in *nøbben* formation seems to be critical, as the oval window ridge is unaffected. This activation may lead to the increased deposition of new endochondral bone, which is mostly composed of calcium phosphate, which is a major component of the bone substance hydroxylapatite. Alternatively, it is possible that the *nøbben* is the result of a signaling defect. Recently, ectopic bone formation between the stapes and styloid process was linked to disrupted noggin/bone morphogenetic protein signaling interactions and conductive hearing loss in $Nog^{+/-}$ mice (54). Furthermore, the underlying molecular events triggering the bone remodeling in the ear might be related to those causing the skeletal abnormalities during development. The delamination of the periosteum seen at 2 weeks of age at the prospective round window ridge might be the result of the neo-ossification.

The crystals found in *Ts* ears display a flat rhomboid-like shape and are reminiscent to cholesterol crystals. This is supported by the observation of cholesterol granulomas in older *Ts* ears. Cholesterol granulomas are an inflammatory response to the presence of foreign bodies, *i.e.* cholesterol crystals, and consist of giant cells, macrophages, and foam cells, and the histology shows typical spindle-like clefts that were filled with cholesterol before it was dissolved during processing of the tissue (55). Clinically, cholesterol crystals and granulomas are associated with middle ear inflammation, but they can also form at other locations of the pneumatized temporal bone, such as in the lateral ventricle and mandible (56–58). There is general agreement that cholesterol crystals are the by-product of cellular degradation. Causes that are being discussed include insufficient drainage, hemolysis, pressure changes, and obstruction of ventilation (55). We do not observe hemorrhage in the 2–36-week-old specimen. It was recently shown that small amounts of cholesterol crystals are sufficient to induce NLRP3 inflammasomes preceding atherosclerotic plaque formations (59). This indicates that cholesterol crystals may at least in part induce the inflammatory response in *Ts*. The cholesterol crystals may initially derive from the tissue breakdown occurring at the round window ridge at 2–3 weeks of age.

The ET plays a critical role in draining and pressurizing the middle ear, and dysfunction of the ET also represents a major cause of OM (60). Given the skeletal malformations that are associated with *Ts* and in particular the abnormalities in the nasal region as also reported by Deol (29), it is perhaps not surprising that the ET is dysmorphic. Interestingly, in contrast to the $Fbxo11^{A2288T}$ (*Jeff*) and $Eya4^{tm1Jse}$ mutants, the ET in *Ts* appears widened. The first signs of inflammation in *Ts* were seen at 2 weeks of age by the dilation and delamination of the periosteum at the prospective round window ridge. Over the next weeks, the inflammation worsened and progressed to a chronic OME. Based upon the histological and audiological data, the phenotype stabilized at around 12 weeks of age. The dysmorphic Eustachian tube may fail to sufficiently drain the middle ear leading to a chronic condition. In this context, it should be mentioned that the lumen of the ET in +/+ mice was more likely to contain cellular debris and clearing products than in *Ts* ETs (preliminary observations). The typical hallmarks of CSOM, bacterial infection and perforation of the eardrum, are not seen. The isolated bacteria are common microbes of the skin flora, whereas bacteria giving rise to CSOM include *Pseudomonas aeruginosa*, *Staphylococcus aureus*, and *Streptococcus pyogenes*, which were not seen in *Ts* ears. We therefore think that the microbes in *Ts* ears do not add significantly to the inflammation.

Our auditory data suggest that hearing loss in *Ts* is a conductive type hearing loss. This classification is based on the significant middle ear pathology in the presence of normal endocochlear potentials and unremarkable inner ear histology. A progressive reduction of EPs ($<$80 mV) was measured in the *Jeff* mutant ($Fbxo11^{A2288T}$) adding a sensorineural component to the hearing loss (61). Mixed hearing loss is also seen in model systems (experimentally induced *Streptococcus* infections) and humans and is due to a middle ear pathology that has invaded the scala tympani (14, 62). In *Ts*, we attribute the loss of DPOAEs and elevated hearing thresholds to a mechanical defect in the middle ear perhaps by changing the fluid dynamics in the inner ear. It is conceivable that the large clusters of crystals and debris at the round window membrane

obstruct the perilymph in the scala tympani, thereby adversely affecting inner ear mechanics such as the motion of the basilar membrane. Similarly, large amounts of cholesterol crystals and cellular debris may hinder effective vibrations of the middle ear bones.

Acknowledgments—We thank Harold Neely for excellent technical help. We thank Daniel Marcus for advice in measuring endocochlear potentials and Glen Martin for help with the DPOAE measurements. We thank our intra- and extramural colleagues for insightful discussions throughout the course of this project, and we acknowledge the excellent expertise of Dr. Mark Bryant (National Institutes of Health phenotyping service) and Dr. Eric Wawrousek (transgenic core facility, NEI, National Institutes of Health). We also thank Xin-Xing Gu, Doris Wu, and Byung Yoon Choi for their comments on the manuscript.

REFERENCES

1. Sher, A. E. (1971) *Acta Otolaryngol. Suppl.* **285,** 1–77
2. Hawke, M., and Jahn, A. F. (1975) *Arch. Otolaryngol.* **101,** 462–464
3. Frisch, T., Sørensen, M. S., Overgaard, S., and Bretlau, P. (2000) *Ann. Otol. Rhinol. Laryngol.* **109,** 33–39
4. Cureoglu, S., Schachern, P. A., Ferlito, A., Rinaldo, A., Tsuprun, V., and Paparella, M. M. (2006) *Am. J. Otolaryngol.* **27,** 334–340
5. Xu, H. X., Joglekar, S. S., and Paparella, M. M. (2009) *Otol. Neurotol.* **30,** 579–580
6. Ealy, M., and Smith, R. J. (2010) *Hear. Res.* **266**, 70–74
7. Thys, M., and Van Camp, G. (2009) *Otol. Neurotol.* **30,** 1021–1032
8. Tinling, S. P., Nabili, V., and Brodie, H. A. (2005) *Ann. Otol. Rhinol. Laryngol.* **114,** 161–166
9. Morris, K. A., Snir, E., Pompeia, C., Koroleva, I. V., Kachar, B., Hayashizaki, Y., Carninci, P., Soares, M. B., and Beisel, K. W. (2005) *J. Assoc. Res. Otolaryngol.* **6,** 75–89
10. Park, K., Ueno, K., and Lim, D. J. (1992) *Am. J. Otolaryngol.* **13,** 93–100
11. Teele, D. W., Klein, J. O., and Rosner, B. (1989) *J. Infect. Dis.* **160,** 83–94
12. Brookhouser, P. E., Worthington, D. W., and Kelly, W. J. (1993) *Laryngoscope* **103,** 371–378
13. Munker, G. (1981) *Adv. Oto-Rhino-Laryngol.* **27,** 138–143
14. Tos, M. (1989) *Acta Otolaryngol. Suppl.* **457,** 87–93
15. Zheng, Q. Y., Hardisty-Hughes, R., and Brown, S. D. (2006) *Brain Res.* **1091,** 9–15
16. Casselbrant, M. L., Mandel, E. M., Fall, P. A., Rockette, H. E., Kurs-Lasky, M., Bluestone, C. D., and Ferrell, R. E. (1999) *JAMA* **282,** 2125–2130
17. Casselbrant, M. L., Mandel, E. M., Jung, J., Ferrell, R. E., Tekely, K., Szatkiewicz, J. P., Ray, A., and Weeks, D. E. (2009) *BMC Med. Genet.* **10,** 85
18. Daly, K. A., Brown, W. M., Segade, F., Bowden, D. W., Keats, B. J., Lindgren, B. R., Levine, S. C., and Rich, S. S. (2004) *Am. J. Hum. Genet.* **75,** 988–997
19. Hardisty-Hughes, R. E., Tateossian, H., Morse, S. A., Romero, M. R., Middleton, A., Tymowska-Lalanne, Z., Hunter, A. J., Cheeseman, M., and Brown, S. D. (2006) *Hum. Mol. Genet.* **15,** 3273–3279
20. Parkinson, N., Hardisty-Hughes, R. E., Tateossian, H., Tsai, H. T., Brooker, D., Morse, S., Lalane, Z., MacKenzie, F., Fray, M., Glenister, P., Woodward, A. M., Polley, S., Barbaric, I., Dear, N., Hough, T. A., Hunter, A. J., Cheeseman, M. T., and Brown, S. D. (2006) *PLoS Genet.* **2,** e149
21. Depreux, F. F., Darrow, K., Conner, D. A., Eavey, R. D., Liberman, M. C., Seidman, C. E., and Seidman, J. G. (2008) *J. Clin. Invest.* **118,** 651–658
22. Eriksson, P. O., Li, J., Ny, T., and Hellström, S. (2006) *Int. J. Med. Microbiol.* **296,** 501–509
23. Pau, H., Fuchs, H., de Angelis, M. H., and Steel, K. P. (2005) *Laryngoscope* **115,** 116–124
24. Steel, K. P., Moorjani, P., and Bock, G. R. (1987) *Hear. Res.* **28,** 227–236
25. Zheng, Q. Y., Tong, Y. C., Alagramam, K. N., and Yu, H. (2007) *Hear. Res.* **231,** 23–31
26. Morgan, W. C. (1950) *J. Hered.* **41,** 208–215
27. Paterson, H. F. (1980) *J. Exp. Zool.* **211,** 247–256
28. Brotherton, T. W., Chui, D. H., McFarland, E. C., and Russell, E. S. (1979) *Blood* **54,** 673–683
29. Deol, M. S. (1961) *J. Embryol. Exp. Morphol.* **6,** 78–95
30. Ishijima, J., Yasui, H., Morishima, M., and Shiroishi, T. (1998) *Genomics* **49,** 341–350
31. Curtin, J. A., Quint, E., Tsipouri, V., Arkell, R. M., Cattanach, B., Copp, A. J., Henderson, D. J., Spurr, N., Stanier, P., Fisher, E. M., Nolan, P. M., Steel, K. P., Brown, S. D., Gray, I. C., and Murdoch, J. N. (2003) *Curr. Biol.* **13,** 1129–1133
32. Montcouquiol, M., Rachel, R. A., Lanford, P. J., Copeland, N. G., Jenkins, N. A., and Kelley, M. W. (2003) *Nature* **423,** 173–177
33. Hustert, E., Scherer, G., Olowson, M., Guénet, J. L., and Balling, R. (1996) *Mamm. Genome* **7,** 881–885
34. Uchida, K., Koopman, P., Mita, A., Wakana, S., Wright, E., Kikkawa, Y., Yonekawa, H., Moriwaki, K., and Shiroishi, T. (1996) *Mamm. Genome* **7,** 481–485
35. Bénit, L., De Parseval, N., Casella, J. F., Callebaut, I., Cordonnier, A., and Heidmann, T. (1997) *J. Virol.* **71,** 5652–5657
36. Marygold, S. J., Roote, J., Reuter, G., Lambertsson, A., Ashburner, M., Millburn, G. H., Harrison, P. M., Yu, Z., Kenmochi, N., Kaufman, T. C., Leevers, S. J., and Cook, K. R. (2007) *Genome Biol.* **8,** R216
37. Saebøe-Larssen, S., Lyamouri, M., Merriam, J., Oksvold, M. P., and Lambertsson, A. (1998) *Genetics* **148,** 1215–1224
38. Draptchinskaia, N., Gustavsson, P., Andersson, B., Pettersson, M., Willig, T. N., Dianzani, I., Ball, S., Tchernia, G., Klar, J., Matsson, H., Tentler, D., Mohandas, N., Carlsson, B., and Dahl, N. (1999) *Nat. Genet.* **21,** 169–175
39. Doherty, L., Sheen, M. R., Vlachos, A., Choesmel, V., O'Donohue, M. F., Clinton, C., Schneider, H. E., Sieff, C. A., Newburger, P. E., Ball, S. E., Niewiadomska, E., Matysiak, M., Glader, B., Arceci, R. J., Farrar, J. E., Atsidaftos, E., Lipton, J. M., Gleizes, P. E., and Gazda, H. T. (2010) *Am. J. Hum. Genet.* **86,** 222–228
40. Farrar, J. E., Nater, M., Caywood, E., McDevitt, M. A., Kowalski, J., Takemoto, C. M., Talbot, C. C., Jr., Meltzer, P., Esposito, D., Beggs, A. H., Schneider, H. E., Grabowska, A., Ball, S. E., Niewiadomska, E., Sieff, C. A., Vlachos, A., Atsidaftos, E., Ellis, S. R., Lipton, J. M., Gazda, H. T., and Arceci, R. J. (2008) *Blood* **112,** 1582–1592
41. Gazda, H. T., Grabowska, A., Merida-Long, L. B., Latawiec, E., Schneider, H. E., Lipton, J. M., Vlachos, A., Atsidaftos, E., Ball, S. E., Orfali, K. A., Niewiadomska, E., Da Costa, L., Tchernia, G., Niemeyer, C., Meerpohl, J. J., Stahl, J., Schratt, G., Glader, B., Backer, K., Wong, C., Nathan, D. G., Beggs, A. H., and Sieff, C. A. (2006) *Am. J. Hum. Genet.* **79,** 1110–1118
42. Gazda, H. T., Sheen, M. R., Vlachos, A., Choesmel, V., O'Donohue, M. F., Schneider, H., Darras, N., Hasman, C., Sieff, C. A., Newburger, P. E., Ball, S. E., Niewiadomska, E., Matysiak, M., Zaucha, J. M., Glader, B., Niemeyer, C., Meerpohl, J. J., Atsidaftos, E., Lipton, J. M., Gleizes, P. E., and Beggs, A. H. (2008) *Am. J. Hum. Genet.* **83,** 769–780
43. Gazda, H. T., and Sieff, C. A. (2006) *Br. J. Haematol.* **135,** 149–157
44. Warner, J. R., and McIntosh, K. B. (2009) *Mol. Cell* **34,** 3–11
45. Rifkind, R. A., Cantor, L. N., Cooper, M., Levy, J., Maniatis, G. M., Bank, A., and Marks, P. A. (1974) *Ann. N. Y. Acad. Sci.* **241,** 113–118
46. Matsson, H., Davey, E. J., Draptchinskaia, N., Hamaguchi, I., Ooka, A., Levéen, P., Forsberg, E., Karlsson, S., and Dahl, N. (2004) *Mol. Cell. Biol.* **24,** 4032–4037
47. Noben-Trauth, K., Zheng, Q. Y., and Johnson, K. R. (2003) *Nat. Genet.* **35,** 21–23
48. Wool, I. G. (1996) *Trends Biochem. Sci.* **21,** 164–165
49. Khan, D. C., DeGagne, J. M., and Trune, D. R. (2000) *Hear. Res.* **142,** 12–22
50. Kotzias, S. A., and Linthicum, F. H., Jr. (1985) *Am. J. Otol.* **6,** 490–494
51. Nabili, V., Brodie, H. A., Neverov, N. I., and Tinling, S. P. (1999) *Laryngoscope* **109,** 931–935
52. Calvi, L. M., Adams, G. B., Weibrecht, K. W., Weber, J. M., Olson, D. P., Knight, M. C., Martin, R. P., Schipani, E., Divieti, P., Bringhurst, F. R., Milner, L. A., Kronenberg, H. M., and Scadden, D. T. (2003) *Nature* **425,** 841–846

53. Beck, G. R., Jr. (2003) *J. Cell. Biochem.* **90,** 234–243
54. Hwang, C. H., and Wu, D. K. (2008) *Hum. Mol. Genet.* **17,** 844–853
55. Nager, G. T., and Vanderveen, T. S. (1976) *Ann. Otol. Rhinol. Laryngol.* **85,** 204–209
56. Grossi, P. M., Ellis, M. J., Cummings, T. J., Gray, L. L., Fukushima, T., and Sampson, J. H. (2008) *J. Neurosurg.* **108,** 357–360
57. Jang, C. H., Kim, J. S., and Cho, Y. B. (2009) *Yonsei Med. J.* **50,** 585–587
58. Sadé, J., and Teitz, A. (1982) *Am. J. Otol.* **3,** 203–208
59. Duewell, P., Kono, H., Rayner, K. J., Sirois, C. M., Vladimer, G., Bauernfeind, F. G., Abela, G. S., Franchi, L., Nuñez, G., Schnurr, M., Espevik, T., Lien, E., Fitzgerald, K. A., Rock, K. L., Moore, K. J., Wright, S. D., Hornung, V., and Latz, E. (2010) *Nature* **464,** 1357–1361
60. Bluestone, C. D. (1996) *Pediatr. Infect. Dis. J.* **15,** 281–291
61. Hardisty, R. E., Erven, A., Logan, K., Morse, S., Guionaud, S., Sancho-Oliver, S., Hunter, A. J., Brown, S. D., and Steel, K. P. (2003) *J. Assoc. Res. Otolaryngol.* **4,** 130–138
62. Ichimiya, I., Suzuki, M., Hirano, T., and Mogi, G. (1999) *Hear. Res.* **131,** 128–134